The Dynamics of a Partially Mixed Estuary*

W. ROCKWELL GEYER, JOHN H. TROWBRIDGE, AND MELISSA M. BOWEN+

Woods Hole Oceanographic Institution, Woods Hole, Massachusetts

(Manuscript received 15 October 1998, in final form 28 September 1999)

ABSTRACT

Measurements of velocity, density, and pressure gradient in the lower Hudson River estuary were used to quantify the dominant terms in the momentum equation and to characterize their variations at tidal and spring–neap timescales. The vertical momentum flux (assumed to be due mainly to turbulent shear stress) was estimated indirectly, based on the residual from the acceleration and pressure gradient terms. The indirect estimates of stress compared favorably to bottom stress estimates using a quadratic drag law, supporting the hypothesis that the tidal momentum equation involves a local balance between tidal acceleration, pressure gradient, and stress divergence.

Estimates of eddy viscosity indicated that there was significant tidal asymmetry, with flood tide values exceeding ebb values by a factor of 2. As a consequence of the asymmetry, the vertical structure of the tidally averaged stress bore no resemblance to the tidally averaged shear. In spite of the asymmetry of vertical mixing, the tidally averaged, estuarine circulation was found to depend simply on the intensity of bottom turbulence, which could be parameterized by a Rayleigh drag formulation based on the tidal velocity magnitude and the tidally averaged near-bottom flow. This seemingly paradoxical result indicates that the estuarine circulation can be modeled without detailed knowledge of the effective eddy viscosity, only requiring an estimate of the bottom drag coefficient, the tidal forcing conditions, and the baroclinic pressure gradient. A notable characteristic of this solution is an inverse dependence of the estuarine circulation on the amplitude of the tides.

1. Introduction

In a pioneering study of estuarine dynamics, Pritchard (1956) quantified the momentum balance of the James River estuary. Based on measurements of the pressure gradient as well as vertical and temporal variations in velocity, he estimated the tidally averaged shear stress distribution. The conceptual model of estuarine circulation that emerged from this work set the stage for several decades of research in estuaries, highlighted by Hansen and Rattray's (1965) similarity solution and Chatwin's (1976) two-dimensional representation of estuarine circulation. Within this paradigm, the dynamics of the estuarine circulation involve a balance between the pressure gradient induced by the out-estuary surface slope, the baroclinic pressure gradient due to the along-estuary salinity gradient, and the stress associated with the estuarine circulation

$$g\frac{\partial \eta_0}{\partial x} + \frac{g}{\rho}\int \frac{\partial \rho}{\partial x}\,dz = \frac{\partial}{\partial z}\left(K_0\frac{\partial u_0}{\partial z}\right), \qquad (1)$$

where g is the acceleration of gravity, η is the sea surface elevation anomaly, ρ is the density of water, K is the eddy viscosity, u is the along-estuary velocity, and the subscript 0 indicates a tidal average. The influence of tides within this formulation enters only in the value of K_0, the effective eddy viscosity.

However, more recent studies of the tidal variability of estuarine dynamics have brought into question the validity of the notion that the dynamics of the mean estuarine shear flow can be represented by this linear equation, when the tidal variability of the flow and mixing processes would suggest that nonlinearities in the advective terms (Partch and Smith 1978; Iannello 1979; Zimmerman 1980) or in vertical mixing (Jay and Smith 1990) could significantly influence the tidally averaged motions. Based on detailed examination of these complex tidal processes, these authors seriously undermine the idea that mixing coefficients acting on the mean vertical gradients of velocity and salinity can parameterize the influence of the tides.

Jay (1991) introduced the idea of tidal asymmetry,

* Woods Hole Oceanographic Institution Contribution Number 9809.

+ Current affiliation: Center for Astrodynamics Research, University of Colorado, Boulder, Colorado.

Corresponding author address: Dr. W. R. Geyer, MS #12, Woods Hole Oceanographic Institution, Woods Hole, MA 02543.
E-mail: rgeyer@whoi.edu

© 2000 American Meteorological Society

Unauthenticated | Downloaded 06/18/24 05:50 PM UTC

suggesting that the estuarine circulation is not principally driven by the baroclinic pressure gradient but rather by the imbalance of the magnitude of eddy viscosity between flood and ebb. This imbalance results from the weaker stratification, and more intense turbulence, during floods than ebbs. Jay provided evidence that tidal asymmetry is important in the Columbia River estuary, which has particularly strong tidal currents, but his ideas would appear to be relevant in many estuarine environments due to the tidal straining of the salinity field resulting in tidal variation in stratification (Simpson et al. 1990).

Jay's result jeopardizes the classic estuarine paradigm of Pritchard and Hansen and Rattray, for it suggests that the tidally averaged, estuarine shear flow may arise not as a result of the along-estuary salinity gradient but rather as a consequence of tidal processes. Jay's ideas indicate that the problem of estimating the magnitude of the estuarine shear flow, which was thought to be solved in the 1960s, appears to be embedded in the complex problem of determining the tidal variability of the eddy viscosity.

This paper provides additional confirmation for Jay's result, that indeed the magnitude of the mean, estuarine shear cannot be explained by the balance as represented by Eq. (1), based on an effective eddy viscosity acting on the mean shear. Rather, the vertical structure of the mean stress and velocity arise as a result of tidal variations. However, these observations also indicate that there is indeed a simple relationship between the intensity of the estuarine circulation and the tide-induced turbulence, reminiscent of Hansen and Rattray's classical formulation. In fact, it is even simpler in that it does not require any information about eddy viscosity. This surprising result stems from the dominant influence of bottom stress on the tidal and tidally averaged dynamics of partially mixed estuaries, and the relative unimportance of stress across the pycnocline in affecting the estuarine circulation.

This paper is based on a set of observations of currents and water properties in the Hudson River estuary. Indirect estimates of stress, based on vertical integration of the terms in the momentum equation (Bowden and Fairburn 1952), provide estimates of tidal and tidally averaged stresses. These are compared with direct measurements as well as a quadratic drag law to provide a measure of confirmation of the method. The resulting estimates of stress then provide the basis for estimating effective eddy viscosity and for assessing the mechanisms controlling the estuarine circulation. The analysis of the tidally averaged dynamics leads to a simple equation for estimating strength of the estuarine circulation, which may have general application in characterizing the subtidal circulation of estuaries.

2. Methods

a. The field program

The Hudson River estuary extends from New York Harbor 30–100 km up the Hudson River, depending on river discharge conditions (Abood 1974). It is classified as partially mixed, with weak stratification during spring tides and vertical salinity variations of up to 10 psu during neap tides. The river discharge ranges from 100 $m^3\ s^{-1}$ during low discharge to 2000 $m^3\ s^{-1}$ during freshet conditions. Tidal range is 1.2–1.6 m, and tidal velocities are typically 1 $m\ s^{-1}$. This study was conducted in the lower portion of the estuary, adjacent to Manhattan Island (Fig. 1), where the estuary has a relatively uniform width (approximately 1 km) and depth (approximately 15 m).

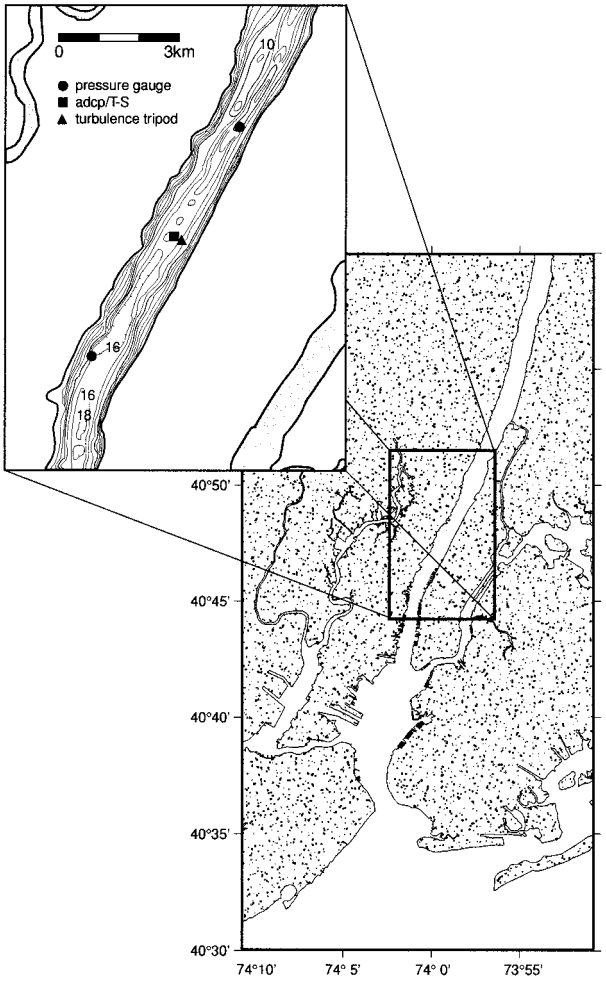

FIG. 1. The Hudson River estuary. Inset shows the position of the moored instruments. Depth contour interval is 2 m.

Measurements were conducted in the estuary during a 2½ month period from August to October 1995. A heavily instrumented, central array was located in the middle of the lower estuary (Fig. 1), in a straight, relatively uniform section. The moored array consisted of an upward-looking, 1.2-mHz acoustic Doppler current profiler (ADCP), a moored array of temperature–conductivity sensors, and a turbulence-measuring tripod as well as an along-channel array of pressure sensors (see Fredericks et al. 1998 for a complete summary).

Unauthenticated | Downloaded 06/18/24 05:50 PM UTC

The ADCP was mounted to a small bottom tripod and deployed in the deepest part of the cross-section at 14.5-m depth. Its transducers were 0.5 m above the bottom, and it provided velocity measurements at 1-m intervals (bins) from 1.5 m to 11.5 m above the bottom. It sampled 200 pings at even intervals once every 10 minutes. The mooring consisted of five Seabird Seacats, located at 2-m intervals between 4.3-m and 12.3-m depth. The Seacats sampled at 5-min intervals. An S4 current meter with temperature and conductivity sensors was located at 2.7-m depth. Pressure sensors were deployed on small bottom tripods at four locations along the thalweg of the lower estuary, including the central site. Seabird Seagauges with Paroscientific pressure gauges and bottom temperature–conductivity sensors were used at each of these pressure measurement locations. The pressure ports were baffled with parallel disks to minimize dynamic pressure effects (see Lentz et al. 1999).

The turbulence-measuring tripod is described in detail in Trowbridge et al. (1999). It included a vertical array of five acoustic current meters capable of resolving turbulent fluctuations to scales of approximately 15 cm. Meteorological data including wind speed and direction, barometric pressure, and relative humidity were measured at an onshore station adjacent to the moored array.

Shipboard measurements included temperature–conductivity–depth (CTD) profiles with an Ocean Sensors CTD and shipboard ADCP measurements on one vessel, as well as microstructure turbulence measurements with a free-falling shear probe (described by Peters and Bockhurst 2000) on another other vessel.

b. Data processing and analysis

This paper focuses on the data from the upward-looking ADCP and pressure gauges, in order to quantify the dominant terms in the along-estuary momentum balance. The precision of the ADCP data was ± 1.5 cm s^{-1} (based on the Doppler resolution and the averaging interval), but there appeared to be some systematic errors of larger magnitude. The bottommost bin appeared to record anomalously high velocities (compared to the nearby turbulence tripod). This was apparently due to flow disturbance by the ADCP tripod. There were also differences between odd and even bins that are probably artifacts of the internal data processing of the ADCP [T. Chereskin (Scripps Institute of Oceanography), 1998 personal communication], originating from the erroneous velocity estimate in the first bin. Based on comparisons with shipboard measurements as well as the nearby turbulence tripod, the bottommost ADCP bin was rejected and the data were averaged between adjacent bins, thereby degrading the vertical resolution to 2-m but obtaining a velocity profile more consistent with the other velocity measurements.

Estimates of vertical momentum flux (or stress) followed the technique of Bowden and Fairburn (1952), based on the assumption that the advective contributions to the stress are negligible, or alternatively that the advective effects can be lumped into an ''effective'' stress. The estimate of stress is based on the vertical integral

$$\tau(z) = -\int_z^h \left(\rho \frac{\partial u}{\partial t} + \frac{\partial p}{\partial x}\right) dz + \tau_s, \qquad (2)$$

where τ is the effective stress, z is the vertical coordinate (positive upward, with $z = 0$ at the bottom), h is the water depth, $\partial p/\partial x$ is the pressure gradient, and τ_s is the surface stress.

The calculation was based on the central site, using the ADCP data for estimates of $\partial u/\partial t$. In order to perform the complete water-column integration, the velocity had to be extrapolated over the top 15% of the water column and the bottom 2 m. The shipboard velocity data, which extended to within 1.5 m of the water surface, indicated the velocity shear decreased approaching the surface. Consistent with these observations, we extrapolated the moored ADCP data to the surface using a parabolic fit that matched the shear at the top bin and curved toward zero shear at the surface. The estimate of stress was insensitive to the form of the extrapolation because it only represented a small fraction of the water column. The extrapolation to the bottom was based on the velocity structure observed at the nearby turbulence tripod, which had measurements at 0.5, 1.0, 2.0, and 3.0 m above the bed and generally exhibited logarithmic profiles. The extrapolation used a tidally varying structure function, the shape of which was determined by the tripod observations, and the amplitude adjusted to match the ADCP velocity at 3.5 m. This method thus preserved tidal phase variations in the velocity structure over the lowest 3 m of the water column, which may have some influence on the momentum integral. In any case, the stress estimates were insensitive to the near-bottom extrapolation because the acceleration term is small relative to the pressure gradient term for small z.

The surface pressure gradient was determined from pressure sensors along the estuary as well as estimates of the baroclinic pressure gradient. The near-bottom pressure gradient was calculated by differencing pressure measurements located 3 km up estuary and down estuary of the central mooring. The upstream pressure sensor was at 22-m water depth, and the downstream gauge was at 18-m depth, whereas the depth at the central mooring was 15 m. These pressure measurements included the contribution of the surface elevation variation as well as the baroclinic contribution, dominated by salinity variations in the estuary. The surface pressure gradient was calculated as follows: first, the pressure at 18-m depth at the deep mooring was estimated by removing the hydrostatic contribution between 18 and 22 m, based on the local measurements of density. Then the baroclinic contribution between the surface and 18 m was removed, based on estimates of the along-estuary salinity gradient (described below). There was

Unauthenticated | Downloaded 06/18/24 05:50 PM UTC

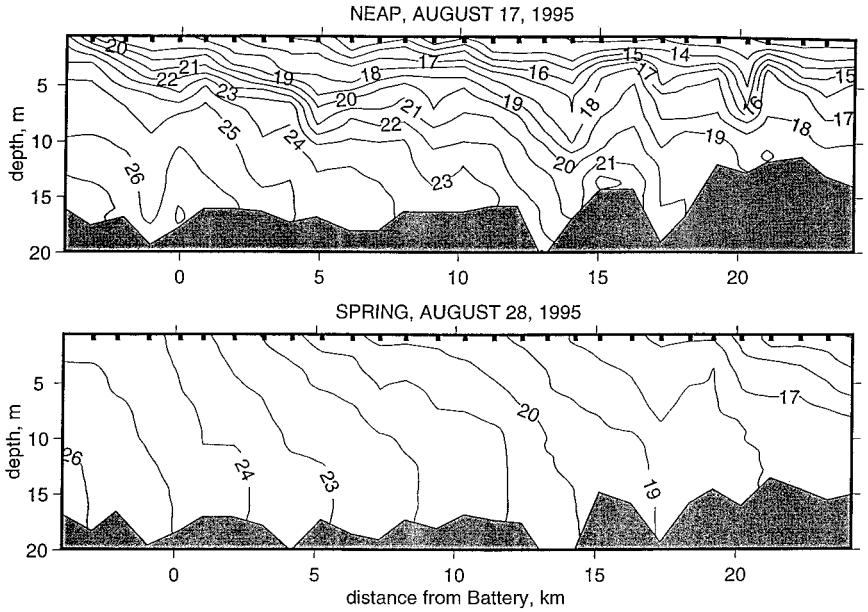

FIG. 2. Cross sections of salinity along the Hudson estuary during neap (upper panel) and spring tides (lower panel) during the 1995 moored observation period. The along-estuary salinity gradient is similar during the two periods, but there is a marked change in the stratification.

still an unknown offset due to the absence of an absolute reference of the heights of the tripods, relative to a local geopotential surface. This offset was readily determined by requiring that the zero-crossings of momentum-integral estimates of bottom stress occur close to times of zero-crossings of bottom velocity.

The baroclinic pressure gradient was first estimated from shipboard observations of along-estuary salinity variation (Fig. 2). However, the estimate was found to vary by a factor of 2 to 4, depending on the horizontal length scale over which the estimates were made and the tidal phase. The variations were particularly pronounced during neap tides, when internal fluctuations sometimes reversed the sign of the baroclinic gradient. A more uniform estimate of the baroclinic gradient was obtained based on tidal variations of the observed salinity at the central mooring. Continuous estimates of the baroclinic pressure gradient were obtained based on integrating the local salt conservation equation, neglecting lateral and vertical advection as well as vertical variations in $\partial s/\partial x$ (as in Uncles and Radford 1980):

$$\frac{\partial \overline{s}}{\partial x} = -\frac{1}{\overline{u}}\frac{\partial \overline{s}}{\partial t} \tag{3}$$

where the overbar indicates a vertical average. For this calculation, only values of $|u|$ exceeding 20 cm s^{-1} were used and the resulting estimates of $\partial\overline{s}/\partial x$ were low-pass filtered to remove the tidal variability of the estimate, which was believed largely to be noise associated with the method. This estimate was found to be consistent (generally to within 20% with no bias) with shipboard measurements obtained at various times through the deployment period (Fig. 3).

The total, depth-varying pressure gradient was estimated at the mooring by combining the measured pressure differences and the estimated baroclinic gradient

$$\frac{\partial p}{\partial x} = \frac{\partial p_{18}}{\partial x} + \beta g\frac{\partial \overline{s}}{\partial x}(h - 18 - z), \tag{4}$$

where $\partial p_{18}/\partial x$ was the pressure gradient at 18 m and $\beta = 0.77 \times 10^{-3}$ is the coefficient of saline expansion.

Surface stress was based on wind measurements, using the bulk formula of Large and Pond (1981). The wind stress was always a small fraction of the bottom stress, even with respect to tidal averages.

3. Results

a. Estuarine conditions

Timeseries of the forcing variables, flow, and salinity in the Hudson estuary are plotted in Fig. 4. The river discharge was low and nearly constant at approximately 100 m^3 s^{-1} (top panel) for most of the deployment due to drought conditions in the watershed. This produced a net outflow of approximately 1 cm s^{-1}. One major discharge event occurred at the end of the deployment. Wind stress was generally weak (second panel), making a small contribution to the dynamics. Tidal velocity amplitude (third panel) varied from 1 to 1.4 m s^{-1} near the surface and from 0.5 to 0.8 m s^{-1} in the bottom water. The monthly modulation of the tides was pronounced during this period due to the coincidence of the apogee

Unauthenticated | Downloaded 06/18/24 05:50 PM UTC

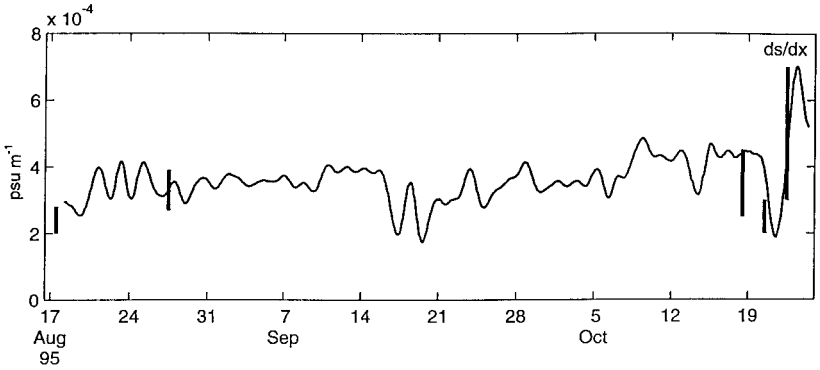

FIG. 3. Estimate of $\partial s/\partial x$ based on Eq. (3) (time series line) and shipboard data (vertical lines). The length of the vertical lines indicates the variability within a tidal cycle.

of the moon's orbit with neap tides. There were three apogean neaps (with unusually low tidal amplitudes) during the period. The low-pass filtered velocity (fourth panel) showed the persistence of the estuarine velocity, with inflow ranging from 0.1 to 0.2 m s^{-1} at the surface and comparable outflow at the bottom. Superimposed on this estuarine circulation were pronounced fluctuations at 2–3 days due to a combination of direct wind forcing and sea level fluctuations. Salinity (bottom panel) was relatively uniform for most of the deployment although the stratification increased markedly during neap tides. The runoff event at the end of the deployment caused a major drop in salinity and also increased stratification.

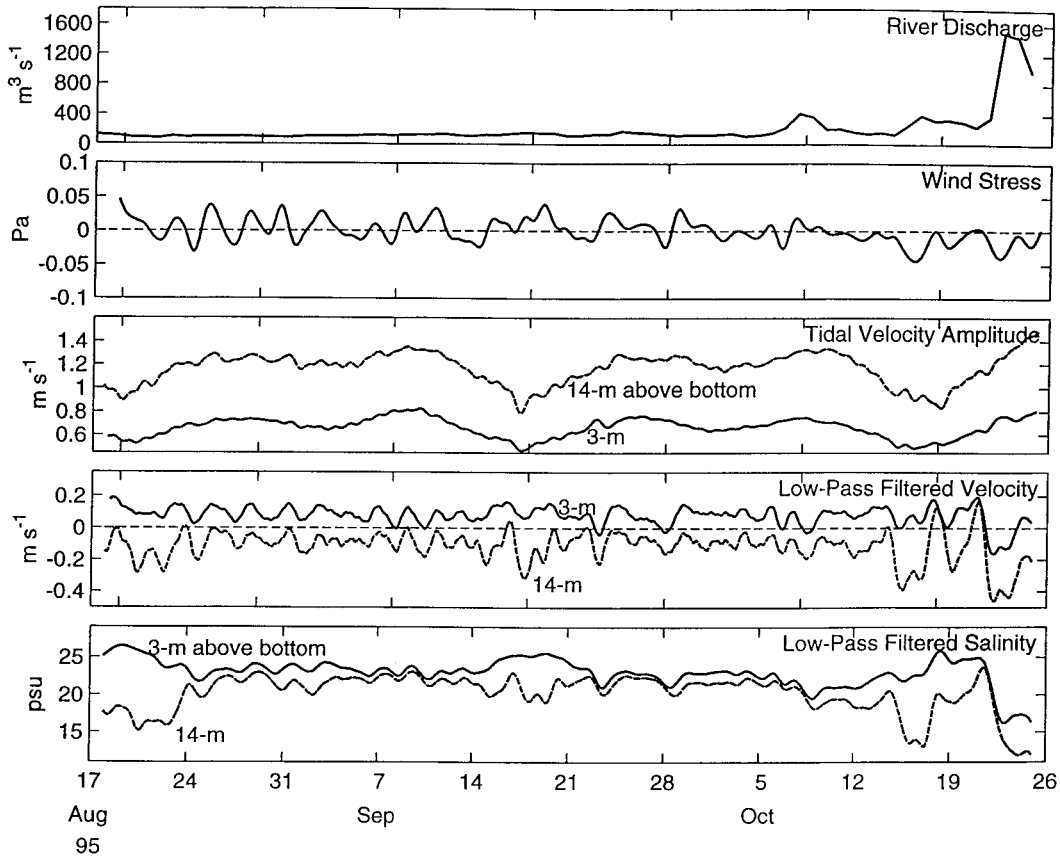

FIG. 4. Time series of river discharge in the Hudson (top panel); along-estuary wind stress (second panel); tidal velocity amplitude (third panel); low-pass filtered, along-estuary velocity (fourth panel); and low-pass filtered salinity (bottom panel). A 33-h filter was used to remove the tidal variability. Monthly modulation of the tidal currents produced variations in shear and stratification. River discharge variations only affected the end of the record.

Unauthenticated | Downloaded 06/18/24 05:50 PM UTC

The lower Hudson estuary had a persistent along-estuary salinity gradient, as shown by salinity sections taken during neap and spring tides (Fig. 2). During both neap and spring tides, the along-estuary salinity gradient was approximately 0.3 psu km^{-1}, although there was spatial and temporal variability (Fig. 3). During neap tides, the surface-to-bottom salinity difference reached 10 psu, while during spring tides the difference was 0–2 psu.

b. The momentum integral

The apparent stress was calculated from Eq. (2) at the central site, using the observations of acceleration, bottom pressure gradient, salinity gradient and wind stress. As a test of the validity of this estimate of tidally varying stress, an estimate of bottom stress was obtained using a quadratic drag law,

$$\tau_b = \rho C_D |u_b| u_b, \tag{5}$$

(where C_D is the bottom drag coefficient and u_b is a near-bottom velocity) and compared to the estimate of stress from Eq. (2). Figure 5 shows a comparison of the bottom stress estimated from the momentum integral with that obtained from a drag law, using the velocity 3.5 m from the bottom (the velocities closer to the bottom were suspect due to interference with the bottom tripod). The regression coefficient $r^2 = 0.91$, indicating that the tidal momentum balance is consistent with Eq. (2), assuming a quadratic drag law. The regression yields a drag coefficient is $3.1 \times 10^{-3} \pm 0.05 \times 10^{-3}$. This is in the expected range of values for mixed sand and mud bottom conditions (Soulsby 1990), which is the typical bed composition at this site in the Hudson.

The estimated offset of the pressure gradient was determined from the linear regression analysis of the integral estimate of bottom stress against the drag-law estimate (Fig. 5), chosen to bring the y intercept of the regression to zero. Based on this analysis, the mean surface pressure gradient was 0.9×10^{-2} Pa m^{-1}, directed seaward. There was a very small difference between springs and neaps. This compares to a mean landward-directed pressure gradient at the bottom of 3.1×10^{-2} Pa m^{-1} due to the baroclinic contribution of the salinity gradient.

The large difference in stratification between spring and neap conditions in the estuary suggested that the dynamics may differ between these two periods, so separate regressions were performed for spring conditions

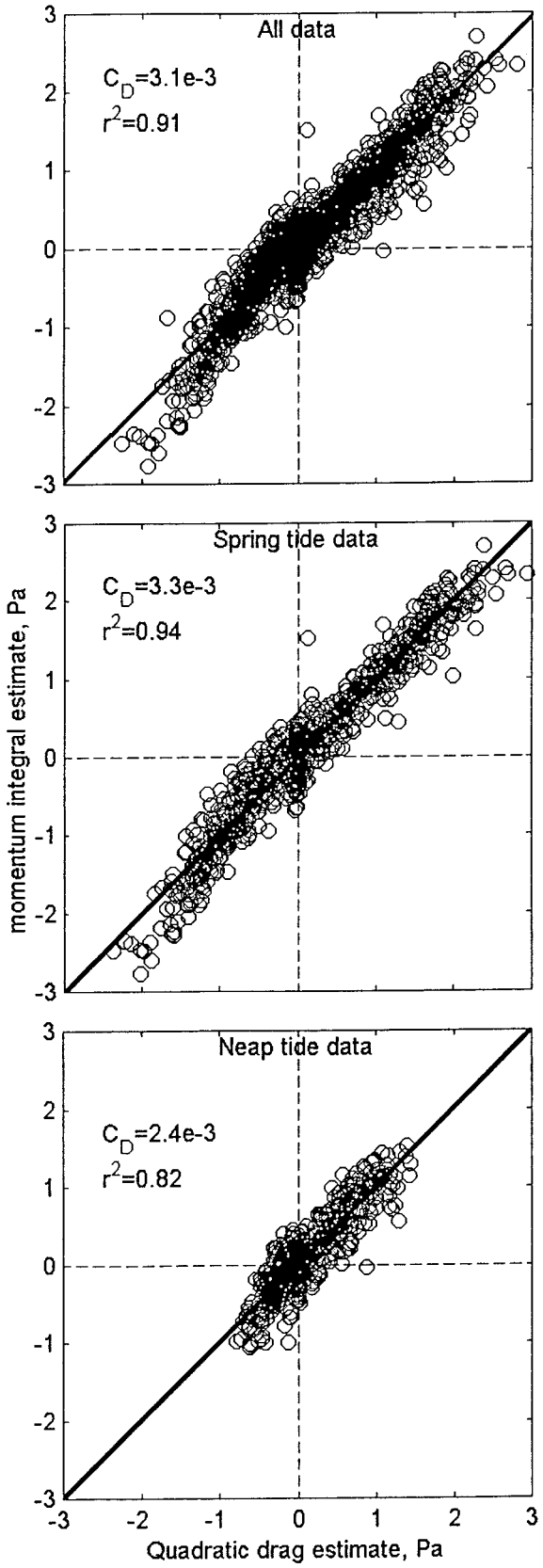

→

FIG. 5. Regression between stress estimates from the momentum integral (vertical axis) and quadratic drag estimates (horizontal axis). The top panel includes all the data, the second panel includes only spring tide data, and the bottom panel includes only neap tide data. The slope of the regression was used to determine the drag coefficient. There is a slight variation in its magnitude between neap and spring tides.

Unauthenticated | Downloaded 06/18/24 05:50 PM UTC

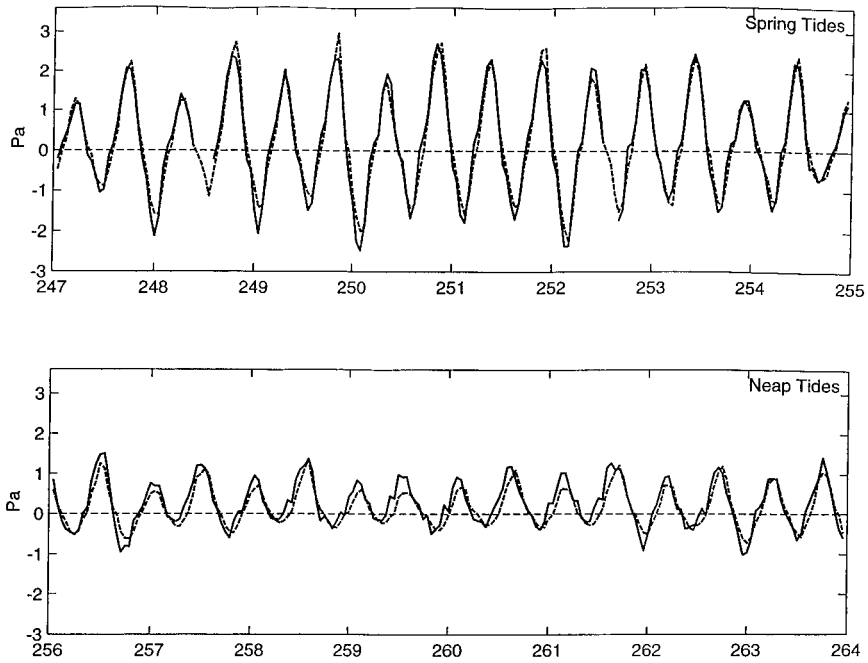

FIG. 6. Time series comparison of the momentum-integral of stress to the drag-law estimate for spring tides (upper panel) and neap tides (lower panel).

(based on the rms stress exceeding 0.7 Pa) and neaps (rms stress less than 0.6 Pa). The results of the regression analysis are shown in the lower panels of Fig. 5. The drag law is satisfied in each case, with a regression coefficient of 0.92 during spring tides and 0.80 during neaps. There is a slight but significant difference in C_D between springs and neaps (3.2×10^{-3} and 2.4×10^{-3}, respectively). This difference may reflect a difference in near-bottom stratification between springs and neaps; however, the gradients were too small and the uncertainty in the measurements too large to quantify the variations.

The spring and neap regression analyses indicate linear behavior during flooding tides, but they both deviate from the linear relationship at maximum ebb, with the momentum integral estimate of stress exceeding the drag coefficient estimate by approximately 20%. This may indicate that there are other sinks of momentum in addition to the local bottom stress, or that the dynamics of the stress–velocity relationship change during maximum ebb.

c. Tidal variations of stress

Timeseries of estimated bottom stress are shown in Fig. 6 for spring and neap conditions, again comparing the momentum integral estimate of stress to a quadratic drag law. During spring tide conditions, the two curves track each other very closely (reflecting the high value of r^2). The only discrepancy occurs around maximum ebb when the momentum integral exceeds the drag law estimate. During neap tides, there is more variability, but the two curves generally track each other well. Note that, during neap tides, the stresses are considerably higher during the flood (positive values) than the ebb due to the influence of the landward residual flow at the bottom.

Vertical profiles of velocity and stress during maximum flood and ebb (Fig. 7) were obtained by averaging all of the data as a function of tidal phase, choosing the observation closest to the time of maximum flow. The error bars were estimated from the statistics of the velocity and pressure measurements, and they do not reflect the additional uncertainty of the assumptions leading to Eq. (2). The ebb velocity profiles are monotonic and strongly sheared during both spring and neap tides. The flood velocity has a subsurface maximum during neap tides, but it is monotonic during springs. The stress profiles show more dramatic differences between neaps and springs, both in magnitude and structure. During neap tides, the stresses are weak in the upper 5 m of the water column, below which they linearly increase toward the bottom. During spring tides, the profiles are nearly linear for the entire water column, indicating significant stress divergence all the way to the surface. The neap stress profiles indicate nearly inviscid conditions in the upper water column, and more so on the flood than the ebb. The reversal in shear during neap, flood tides also suggests that the boundary-generated stress does not reach the surface during that phase of the tide.

The relevance of the eddy viscosity as a means of estimating stress can be assessed by calculating the regression between the stress and shear as a function of

Unauthenticated | Downloaded 06/18/24 05:50 PM UTC

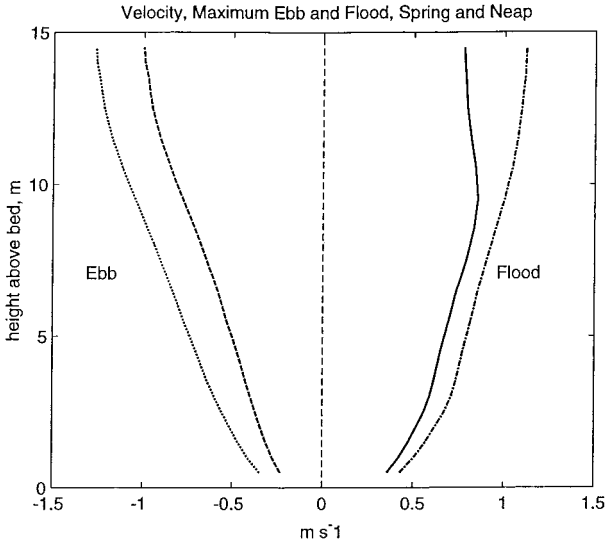

FIG. 7. Vertical profiles of tidal velocity (upper panel) and stress (lower panel) for maximum flood and ebb conditions during spring and neap tides. The larger magnitudes of velocity and stress correspond to spring tide conditions. The error bars on the stress were calculated from the standard errors of the four ensembles of stress estimates, assuming that each tidal cycle is an independent realization. Note that the stress nearly vanishes in the upper water column during neap tides.

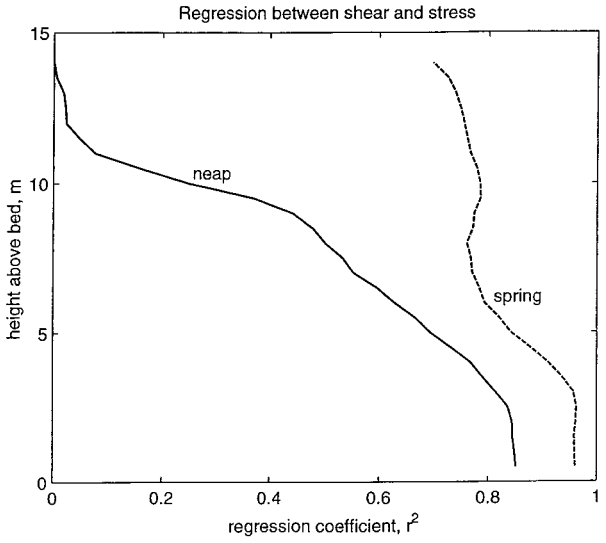

FIG. 8. Regression between tidally varying shear and stress, for neap conditions (solid line) and spring (dashed line). A high regression coefficient supports the use of an eddy viscosity formulation to represent stress. The shear is clearly not a good predictor of stress in the upper water column during neap tides, but otherwise there is a strong correlation.

the vertical position (Fig. 8). During spring tides, virtually all of the variance in stress explained by the variability in shear in the lowest 3 m of the water column, and the regression coefficient remains high through the water column, indicating that the eddy viscosity provides a reasonable model for stress variations. During neap tides, the regression values are high in the lowest 4 m (although not as high as spring-tide values, and they drop off monotonically, approaching zero for the upper 3 m of the water column. During neaps, an eddy viscosity is appropriate for the lower water column, but other processes (such as stratification; see below) cause a decorrelation of shear with stress in the upper water column.

Eddy viscosity was estimated for the maximum flood and ebb conditions for spring and neap tides (Fig. 9) based on the quotient of the tidal-phase-averaged stress with the shear. The viscosity is approximately three times larger during spring tides than neaps, and it is roughly twice as large during floods than ebbs. The latter condition is an indication of tidal asymmetry (Jay 1991; see below for further discussion). The maximum viscosity occurs only 3–4 m above the bottom, in the well-mixed part of the boundary layer. The peak magnitude of the viscosity during spring, flood tides approaches the magnitude for unstratified, open channel flow (e.g., Nezu and Rodi 1986):

$$K = \kappa u \cdot z(1 - z/h), \tag{6}$$

where κ is von Kármán's constant ($\sim$0.4) and h is the water depth. Even the maximum viscosities for the other three cases are attenuated by $\sim$50% from the neutral value. Higher in the water column, all of the profiles are attenuated by 60%–95% from the neutral value. These deviations from a neutral viscosity are likely due to the influence of stratification, which is strongest during neap tides when the attenuation is most apparent.

For the neap, flood case, the eddy viscosity becomes singular at 9 m, where the shear changes sign, and it is negative above that level. In this part of the domain, processes other than turbulent momentum flux, such as vertical and lateral advection, apparently make up the

Unauthenticated | Downloaded 06/18/24 05:50 PM UTC

deficit in the momentum balance. The unrealistic values of eddy viscosity were not plotted in Fig. 9.

The gradient Richardson number distribution (based on phase-averaged velocity and density; Fig. 9b) indicates low Richardson numbers in the bottom boundary layer for all tidal conditions and stable conditions in the upper water column (Ri $>$ 0.25) for all but the spring, ebb flow. The lowest Richardson numbers in the bottom boundary layer occur during the flooding tide, consistent with the higher values of eddy viscosity at those times.

d. Tidally averaged stress

The tidally averaged stress was found to be nearly identical for spring and neap tides (Fig. 10). It is dominated by the flood-directed stress, with a slight stress reversal in the top 5 m of the water column in the direction of the ebb stress. This result is surprising in light of the substantial variation in the magnitude and vertical structure of the tidal stress between springs and neaps, as indicated in Figs. 5, 6, and 7. This apparent paradox is explained as follows: the large, oppositely directed, ebb and flood stresses during spring tides nearly cancel each other out, yielding the same tidal average as the substantially smaller but more asymmetric stresses of neap tides (Fig. 7). This asymmetry results from an increase in the estuarine circulation (or exchange flow) during neap tides (Fig. 10, upper panel). The similarity in the mean stress between springs and neaps indicates that tidally averaged, baroclinic and barotropic pressure gradients are the same during spring and neap tides [Eq. (4): note that acceleration is negligible for the tidally averaged equation].

The vertical structure of the mean stress and the mean velocity structure in Fig. 10 clearly indicate that the mean, estuarine dynamics cannot be represented by a time-invariant eddy viscosity; rather, tidal asymmetry must be invoked to explain the tidally averaged quantities. The shear changes sign several meters above the bottom, but the stress changes sign near the water surface. Furthermore, the strong, mean shears in the vicinity of the pycnocline (particularly during neap tides) correspond to weak mean stresses. This mismatch between mean shear and mean stress is clear evidence of tidal asymmetry. More intense vertical mixing during the flood (Fig. 9, upper panel) produces more stress than the more strongly sheared ebb, so the tidally averaged stress profile is dominated by the flood conditions for most of the water column.

In order to determine whether the tidally averaged bottom stress could be related to the tidally averaged, near-bottom velocity, a linearized drag law was tested, based on the magnitude of the tidal velocity and the subtidal velocity

$$\tau_0/\rho = Ru_0, \tag{7a}$$

where

$$R = \alpha C_D u_T \tag{7b}$$

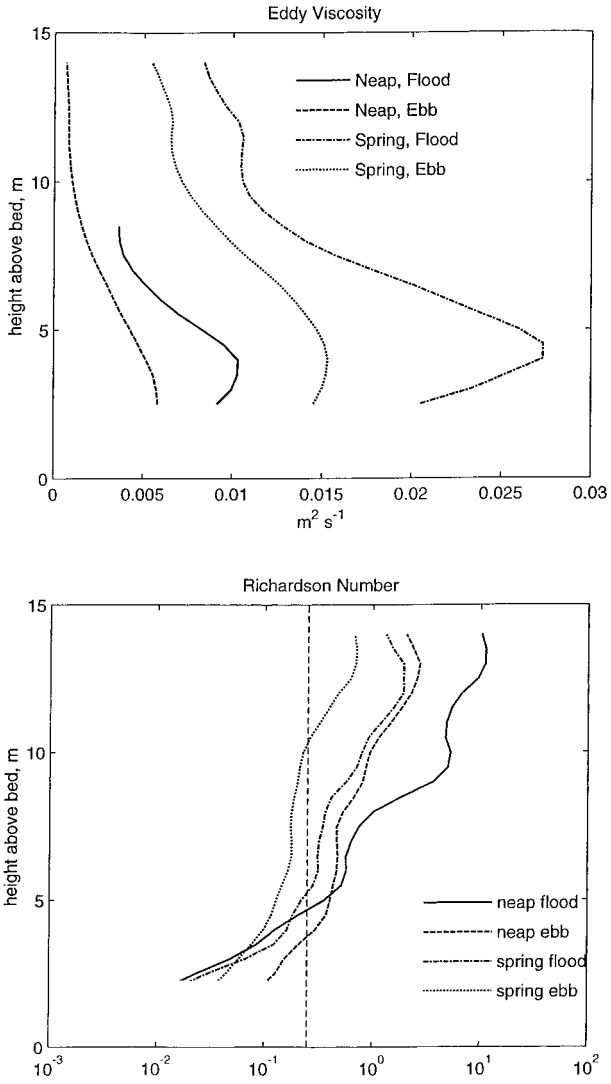

FIG. 9. Estimates of eddy viscosity based on the velocity and stress distributions shown in Fig. 7 (upper panel). The eddy viscosity becomes unphysical in the upper water column for flood, neap tides because of the change in sign of the shear, so that portion was not plotted. Estimates of gradient Richardson number Ri $= (-\rho^{-1}g\partial\rho/\partial x)/(\partial u/\partial z)^2$ for the same conditions (lower panel). The stability threshold of 0.25 is indicated with a dashed line. Mixing is inhibited for Ri $>$ 0.25.

and τ_0 is the tidally averaged stress, R is a Rayleigh drag factor, u_0 is the tidally averaged, near-bottom velocity, α is a constant of integration ($\sim$2) that comes from tidal averaging of the expression $|\cos\varphi + \varepsilon|(\cos\varphi + \varepsilon)/\varepsilon$ (where φ is tidal phase and ε is a small parameter representing the ratio of mean velocity to tidal velocity), C_D is the drag coefficient based on the tidal variations of stress (including the spring–neap variation in magnitude), and u_T is the rms tidal velocity (at 3 m above bottom for this calculation). This linearized estimate of bottom stress was compared to the momentum integral estimate (Fig. 11) with surprisingly good results. Not

Unauthenticated | Downloaded 06/18/24 05:50 PM UTC

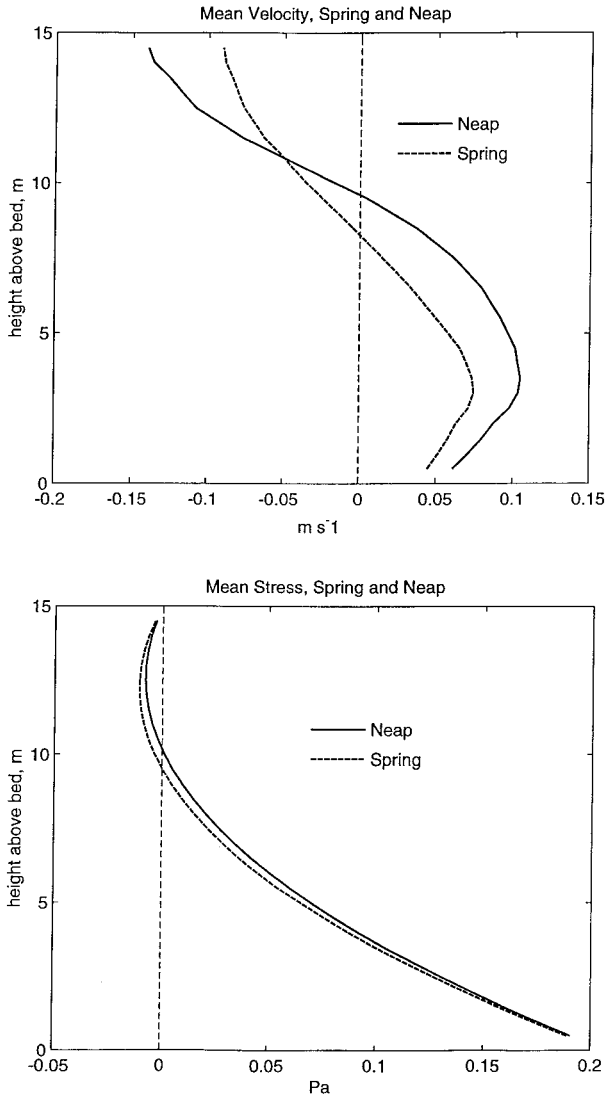

FIG. 10. Tidally averaged velocity (upper panel) and stress profiles (lower panel) during neap and spring tides. The estuarine exchange flow is evident in both neap and spring conditions, although it is stronger during neaps. The tidally averaged stress distribution is virtually the same between neaps and springs, even though the tidal stresses are considerably different.

only was the mean stress well estimated by the linear drag law, but the fluctuations were faithfully reproduced as well with nearly 80% of the variance in subtidal bottom stress being explained by the linear drag law.

There are several important implications of this finding. First, although tidal asymmetry of K affects the relationship between mean shear and mean stress throughout most of the water column, the bottom drag coefficient is roughly the same between flood and ebb, yielding a simple relationship between tidally averaged, near-bottom velocity and tidally averaged bottom stress. Second, this result suggests that the linear momentum balance that was assumed for the calculation of bottom stress is consistent with the tidally averaged dynamics. This is particularly significant because of the potential dominance of slight nonlinearies in the tidal dynamics on the subtidal frequencies (Nihoul and Ronday 1975; Zimmerman 1986) in which the forcing terms are an order of magnitude smaller than the forcing terms at tidal frequencies. The consistency of linear dynamics with the low-frequency response in this system suggests that there is little rectification of tidal nonlinearities into the subtidal dynamics.

The large fluctuations in bottom stress evident in Fig. 11 reflect the variability of the near-bottom velocity, which are mostly due to barotropic variations in flow at timescales of 2–3 days. These fluctuations are significantly correlated with fluctuations in sea level ($r^2 = 0.32$, 30 degrees of freedom) and weakly correlated with local winds. These fluctuations only rarely reverse the sign of the bottom stress, which is on average directed landward with a magnitude of 0.2 Pa. The only significant seaward-directed bottom stress occurred during the runoff event at the end of the deployment (cf. Fig. 4) when there was a strong, barotropic outflow due to the combination of river flow and sea-level forcing.

4. Discussion

a. Comparison with turbulence measurements

The turbulence tripod located near the central mooring provides an independent estimate of near-bottom stress (and thus C_D), based on direct measurements of Reynolds stress by the correlation of horizontal and vertical velocity fluctuations (Trowbridge et al. 1999). The direct measurements of stress were found to be approximately 20% smaller than the momentum integral estimates during neap tides, and as much as 50% smaller during spring tides.

The stress estimates from the momentum balance were also compared with the microstructure measurements of turbulent dissipation by Peters and Bokhurst (2000). These measurements were performed from a vessel moving slowly with the current through the region of the moored measurements, providing a spatial average of the dissipation within 1 km up- and downestuary of the mooring. The turbulence production $\rho^{-1}\tau\partial u/\partial z$ should nearly balance the dissipation ε (Tennekes and Lumley 1972), at most exceeding it by 15% when buoyancy flux is maximal (Osborn 1980). The turbulence production based on the indirect estimates of stress and measured shear could thus be compared to the dissipation observations. The best agreement occurred during spring tide ebb conditions, when the two approaches yielded values within 20%–40% of each other (compared to variations of several orders of magnitude), with peak values around 1.0×10^{-4} m^2 s^{-3}. The comparison showed more scatter during other periods, the production and dissipation estimates generally falling within a factor of 3–5 of each other. One period of significant discrepancy was neap ebb tides, during

Unauthenticated | Downloaded 06/18/24 05:50 PM UTC

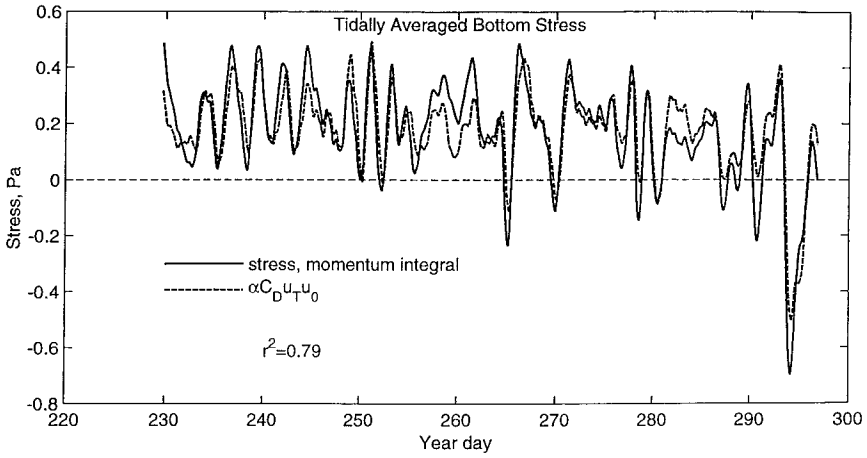

FIG. 11. Comparison of low-pass filtered bottom stress estimate to the bottom drag law from Eq. (7). The amplitude as well as fluctuations of stress are well represented by this Rayleigh drag formulation.

which the microstructure measurements in the middle and upper water column indicated values $<10^{-6}\,\mathrm{m^2\,s^{-3}}$, whereas the production estimates were an order of magnitude greater. This discrepancy may be explained by heterogeneity of mixing during neap tides that is not reflected in the indirect stress estimates, which effectively integrate over the 6-km separation of the pressure sensors.

The comparison with these two different turbulence measurement techniques is not conclusive; it certainly leaves open the possibility that other processes besides local, turbulent stress divergence make up a fraction of the momentum balance. Spatial variability of stress may account for the persistent differences between the turbulence tripod and the momentum integral estimates and some of the deviations from the microstructure measurements. It is also possible that advective processes, such as secondary flows, play an important role in the momentum balance. In order to be consistent with the drag law results, these advective contributions have to scale quadratically with the tidal velocity. Moreover, their contribution must occur at spatial scales smaller than the separation between the pressure sensors, that is, at scales less than 6 km. Secondary flows (Smith 1976; Nunes and Simpson 1985; Kalkwijk and Booij 1986; Geyer 1993) would provide additional momentum flux in the same sense as the stress, and the observations of lateral velocities are not precise enough to rule out their potential contribution to the momentum balance (see Trowbridge et al. 1999 for further discussion.) In any case, the momentum balance is well represented by an ''effective drag'' law, whether it represents simply the contribution of turbulent stress or a combination of turbulence and organized flow structures within the estuary.

b. Tidal asymmetry

This study provides an observational verification of the tidal asymmetry mechanism of Jay (1991) in that the tidal fluctuations in vertical mixing have an important influence on the tidally averaged vertical structure of stress and shear. The mean stress can be represented as a sum of two gradient transport terms, one representing the mean and the other representing the tidal fluctuations

$$\overline{\tau/\rho} = \overline{K}\frac{\partial \overline{u}}{\partial z} + \overline{\tilde{K}\frac{\partial \tilde{u}}{\partial z}}, \tag{8}$$

where the overbar indicates a tidal average, and the tilde represents the tidal variations about that average. Based on these observations, the first term accounts for about half of the mean stress near the bottom, but for most of the water column the mean stress is dominated by the oscillatory term. The variations in K are due in part to higher bottom stresses during the flood than the ebb (due simply to the higher near-bottom velocities on flood than ebb). In addition, the lower half of the water column is more weakly stratified during floods than ebbs, which allows more energetic turbulence in the lower part of the water column during floods (cf. Fig. 9b).

The key importance of tidal asymmetry appears to be in the vertical distribution of stress: the high stresses in the thick boundary layer during the flood tide tend to dominate the stress distribution, even though shears are much more pronounced during the ebb. This asymmetry has the important consequence that the tidally averaged stress is small in the upper part of the water column throughout the spring–neap cycle, even though the instantaneous stress is large during spring tides. The more intense mixing during flood tides compensates for the weaker shears, so the stresses are nearly equal and op-

Unauthenticated | Downloaded 06/18/24 05:50 PM UTC

posite between flood and ebb, even though there is a net outflow in the upper layer. This result has important implications for estuarine dynamics, as indicated in the following section.

c. A simple equation for the estuarine circulation

The estuarine circulation is one of the most fundamental and important quantities in an estuary because it determines the salt flux and horizontal dispersion and is one of the key variables affecting stratification. The results of this study hold promise for estimating the estuarine circulation because they suggest that the magnitude of the stress between the bottom inflow and surface outflow may not be large enough to have significant influence on the dynamics. If this is the case, then the eddy viscosity no longer plays a crucial role in determining the strength of the circulation because the only significant stress term is in the bottom boundary layer. It has been shown that the bottom stress is readily parameterized by a Rayleigh drag law, so the solution for the estuarine circulation should be straightforward.

A two-layer model of the vertical structure of an estuary is based on the tidally averaged velocity and stress distributions (Fig. 10), which indicate that the zero-crossing of stress is close to the zero-crossing of velocity, providing a convenient separation of the upper and lower layers. Lateral and along-estuary variations are neglected, except that a uniform along-estuary salinity gradient is imposed. The layer-averaged equations for the subtidal motions are

$$\frac{\partial u_1}{\partial t} = -g\frac{\partial \eta}{\partial x} - \frac{h_1}{2}\frac{g}{\rho}\frac{\partial \rho}{\partial x} \tag{9}$$

$$\frac{\partial u_2}{\partial t} = -g\frac{\partial \eta}{\partial x} - \frac{(h + h_1)}{2}\frac{g}{\rho}\frac{\partial \rho}{\partial x} - R\frac{u_2}{h_2}, \tag{10}$$

where u_1 and u_2 are layer averaged velocities in the upper and lower layers respectively, h_1 and h_2 are layer thicknesses, and again R is a Rayleigh friction velocity. Stress at the free surface has been neglected, and the stress between the upper and lower layers is set to zero, based on the mean stress profile (Fig. 10). Note that Eq. (9) is inviscid as a consequence of the choice of the boundary between the upper and lower layers. Defining an estuarine exchange velocity $\Delta u = u_2 - u_1$, Eqs. (9) and (10) are combined to yield an equation for the exchange velocity

$$\frac{\partial(\Delta u)}{\partial t} = -\frac{h}{2}\frac{g}{\rho}\frac{\partial \rho}{\partial x} - R\frac{u_2}{h_2}. \tag{11}$$

At timescales longer than several days, the acceleration term is negligible compared to the other two terms. In addition, for timescales longer than those of meteorological fluctuations, the barotropic flow is equal to the river flow. Neglecting the effects of lateral variations in depth, the two-layer continuity equation can be used to obtain an additional expression for Δu in terms of the lower layer velocity and freshwater outflow:

$$\Delta u = (u_2 - u_r)\frac{h}{h_1}, \tag{12}$$

where u_r is the river outflow velocity, which is much smaller than u_2 except during extreme discharge conditions. Neglecting u_r, Eqs. (9) and (10) can be combined to obtain an expression for Δu as a function of the baroclinic pressure gradient and R:

$$\Delta u = -\frac{1}{2R}\frac{h^2 h_2}{h_1}\frac{g}{\rho}\frac{\partial \rho}{\partial x}. \tag{13}$$

This expression is virtually identical to that derived by Godfrey (1980) for estuarine circulation; however, his parameterization of the Rayleigh friction velocity represented the stress between the upper and lower layers rather than the bottom stress as formulated here.

The value of Δu was calculated based on estimates of $h = 15$ m, $h_1 = 7$ m, $h_2 = 9$ m, R from Eq. (7b) and $\rho^{-1} g d\rho/dx$ from time series estimates of ds/dx, and plotted in Fig. 12. This equation approximates well the record-mean estimate of velocity difference as well as most of its low-frequency variability. The spring–neap variations in the exchange flow are well represented by Eq. (13) due to the inverse dependence on R. Note that most of the variability of R comes from variations in tidal amplitude; an additional 10% variation comes from variation in C_D. The 2–3 day fluctuations are not captured due to the neglected contributions of wind stress as well as short-term barotropic and baroclinic fluctuations.

Equation (13) provides the surprising result that the exchange flow does not depend on mixing of momentum across the pycnocline, but only on the tidally averaged bottom stress. This result stems from the fact that the tidally averaged stress vanishes in the vicinity of the pycnocline. This means that the strength of the estuarine circulation can be predicted simply from a knowledge of the bottom boundary layer conditions, without requiring an estimate of the highly variable eddy viscosity within the stratified interior (cf. Fig. 9). A priori, one would expect that the strength of the estuarine circulation would be a sensitive function of stratification because of its influence on the magnitude of the eddy viscosity (Munk and Anderson 1948; Mellor and Yamada 1987). However, because the zero-crossing of tidally averaged stress is in the middle of the pycnocline, the estuarine circulation is quite insensitive to the eddy viscosity structure.

These results are valid over a broad range of stratification conditions; there is a ten-fold change in stratification between neap and spring tides in the Hudson River. Stratification does not vanish during spring tides, however. If the water were completely mixed, tidal asymmetry would not occur, and there would be a significant tidally averaged stress between the upper and

Unauthenticated | Downloaded 06/18/24 05:50 PM UTC

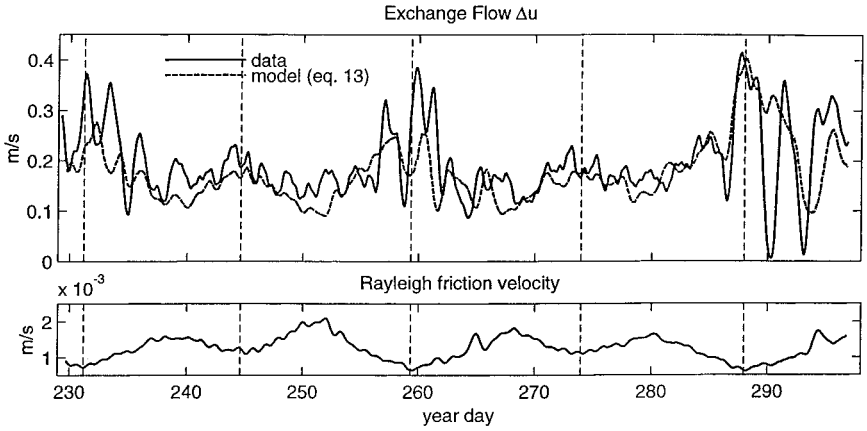

FIG. 12. Observations of exchange flow Δu, compared with model estimates from Eq. (13). The Rayleigh friction velocity is shown in the lower panel. Neap tides are indicated by vertical dashed lines. Maximum exchange flow occurs during neap tides, which correspond to minima in the Rayleigh friction velocity. The average value of the exchange flow and its spring–neap variability are well represented by the model. Short-term fluctuations in exchange flow are not resolved, because of the neglect of fluctuations of the barotropic flow.

lower layers. This would result in a two–fourfold decrease in the magnitude of Δu relative to Eq. (13), assuming that the internal stresses would be comparable to the bottom stress. Another factor affecting the magnitude of Δu is the estuarine geometry. The lower Hudson estuary has very limited lateral shoals and a roughly U-shaped cross section. An estuary with more extensive shoals would have relatively more bottom stress affecting the upper layer, and the exchange flow would likely be reduced from the value obtained in Eq. (13).

5. Summary and conclusions

This study demonstrates that the tidal and subtidal momentum balances in a straight section of the Hudson River estuary can be explained by a local balance between time dependence, pressure gradient, and stress divergence, based on a quadratic drag law for bottom stress. There are discrepancies in these estimates of stress with those of a nearby turbulence-measuring tripod, which might indicate spatial variability of stress or unresolved contributions of advection to the momentum balance. Nevertheless, the tidal and low-frequency momentum balance can be closed with an effective bottom drag law, which has important implications on the tidally averaged momentum balance.

A simple expression can be formulated for the estuarine exchange flow, based on a representation of bottom drag by a Rayleigh friction velocity and the empirical result that the stress vanishes in the vicinity of the pycnocline. This formulation, represented by Eq. (13) accurately reproduces magnitude and spring–neap variability of the estuarine exchange flow in the Hudson estuary. It is surprising that a simple, linear expression would apply in a regime where there is a large tidal asymmetry in eddy viscosity. However, the asymmetry in vertical mixing maintains low values of tidally averaged stress across the sheared pycnocline, which decouples the estuarine exchange flow from internal mixing processes. Equation (13) provides a similar result to the Hansen and Rattray (1965) formula for the estuarine circulation, without the intractable problem of specifying a tidally averaged eddy viscosity.

Acknowledgments. The authors thank Sandy Williams and Janet Fredericks for their help in the instrumentation and data processing, respectively. Two anonymous reviewers provided helpful suggestions. This work was supported by National Science Foundation Grant OCE94-15617 and Hudson River Foundation Grant 002/94P.

REFERENCES

Abood, K. A., 1974: Circulation in the Hudson estuary. *Hudson River Colloquium,* O. A. Roels, Ed., Annals of the New York Academy of Sciences, Vol. 250, New York Academy of Sciences, 38–111.

Bowden, K. F., and L. A. Fairbairn, 1952: A determination of the frictional forces in a tidal current. *Proc. Roy. Soc. London A,* **214,** 371–392.

Chatwin, P. C., 1976: Some remarks on the maintenance of the salinity distribution in estuaries. *Estuarine Coastal Mar. Sci.,* **4,** 555–566.

Fredericks, J. J., J. H. Trowbridge, W. R. Geyer, A. J. Williams III, M. Bowen, and J. Woodruff, 1998: Stress, salt flux, and dynamics of a partially mixed estuary. WHOI Tech. Rep. WHOI-98-17, 133 pp. [Available from WHOI, Woods Hole, MA 02543.]

Geyer, W. R., 1993: Three-dimensional tidal flow around headlands. *J. Geophys. Res.,* **98** (C1), 955–966.

Godfrey, J. S., 1980: A numerical model of the James River estuary, Virginia, U.S.A. *Estuarine Coastal Mar. Sci.,* **11,** 295–310.

Hansen, D. V., and M. Rattray Jr., 1965: Gravitational circulation in straits and estuaries. *J. Mar. Res.,* **23,** 104–122.

Ianniello, J. P., 1979: Tidally induced residual currents in estuaries of variable breadth and depth. *J. Phys. Oceanogr.,* **9,** 962–974.

Jay, D. A., 1991: Measurements and modeling of the spatial structure

Unauthenticated | Downloaded 06/18/24 05:50 PM UTC

of nonlinear tidal flow around a headland. *Tidal Hydrodynamics*, B. B. Parker, Ed., John Wiley and Sons, 403–418.

——, and J. D. Smith, 1990: Residual circulation in shallow estuaries, 2: Weakly stratified and partially mixed, narrow estuaries. *J. Geophys. Res.*, **95,** 733–748.

Kalkwijk, J. P. T., and R. Booij, 1986: Adaptation of secondary flow in nearly-horizontal flow. *J. Hydraulic Eng.*, **24,** 19–37.

Large, W. G., and S. Pond, 1981: Open ocean momentum flux measurements in moderate to strong winds. *J. Phys. Oceanogr.*, **11,** 324–336.

Lentz, S., R. T. Guza, F. Feddersen, and T. H. C. Herbers, 1999: Momentum balances on the North Carolina inner shelf. *J. Geophys. Res.*, **104,** 18 205–18 226.

Mellor, G. L., and T. Yamada, 1982: Development of a turbulence closure model for geophysical fluid problems. *Rev. Geophys. Space Phys.*, **20,** 851–875.

Munk, W. H., and E. R. Anderson, 1948: Notes on a theory of the thermocline. *J. Mar. Res.*, **7,** 276–295.

Nezu, I., and W. Rodi, 1986: Open-channel flow measurements with a laser Doppler anemometer. *J. Hydraulic Eng.*, **112,** 335–355.

Nihoul, J. C. J., and F. C. Ronday, 1975: The influence of the ''tidal stress'' on the residual circulation. *Tellus*, **27** (5), 484–490.

Nunes, R. A., and J. H. Simpson, 1985: Axial convergence in a well-mixed estuary. *Estuarine Coastal Shelf Sci.*, **20,** 637–649.

Osborn, T. R. J., 1980: Estimates of the local rate of vertical diffusion from dissipation measurements. *J. Phys. Oceanogr.*, **10,** 83–89.

Partch, E. N., and J. D. Smith, 1978: Time dependent mixing in a salt wedge estuary. *Estuarine Coastal Mar. Sci.*, **6,** 3–19.

Peters, H., and R. Bokhorst, 2000: Microstructure observations of turbulent mixing in a partially mixed estuary, Part I: Dissipation rate. *J. Phys. Oceanogr.*, **30,** 1232–1244.

Pritchard, D. W., 1956: The dynamic structure of a coastal plain estuary. *J. Mar. Res.*, **15,** 33–42.

Simpson, J. H., J. Brown, J. Matthews, and G. Allen, 1990: Tidal straining, density currents, and stirring in the control of estuarine stratification. *Estuaries*, **13,** 125–132.

Smith, R., 1976: Longitudinal dispersion of a buoyant contaminant in a shallow channel. *J. Fluid Mech.*, **78,** 677–688.

Soulsby, R. L., 1990: Tidal-current boundary layers. *The Sea*. Vol. 9: *Ocean Engineering Science*, B. Le Mehaute and D. M. Hanes, Eds., Wiley and Sons, 523–566.

Tennekes, H., and J. L. Lumley, 1972: *A First Course in Turbulence*. The MIT Press, 300 pp.

Trowbridge, J. H., W. R. Geyer, M. M. Bowen, and A. J. Williams III, 1999: Near-bottom turbulence measurements in a partially mixed estuary: Turbulent energy balance, velocity structure, and along-channel momentum balance. *J. Phys. Oceanogr*, **29,** 3056–3072.

Uncles, R. J., and P. J. Radford, 1980: Seasonal and spring-neap tidal dependence of axial dispersion coefficients in the Severn a wide, vertically mixed estuary. *J. Fluid Mech.*, **98,** 703–726.

Zimmerman, J. T. F., 1980: Vorticity transfer by tidal currents over an irregular topography. *J. Mar. Res.*, **38** (4), 601–630.

——, 1986: The tidal whirlpool: A review of horizontal dispersion by tidal and residual currents. *Netherlands J. Sea Res.*, **20** (2/3), 133–154.

Unauthenticated | Downloaded 06/18/24 05:50 PM UTC